Shock-wave experiments at threefold compression

Charles E. Ragan III
Los Alamos National Laboratory, Los Alamos, New Mexico 87545
(Received 3 June 1983)

A high-pressure shock wave generated by an underground nuclear explosion was used to obtain precise Hugoniot data from impedance-matching measurements at pressures ranging from 1 to 6 TPa and corresponding to threefold compressions. The shock passed from a 180-mm-diam by 17.5-mm-thick lead driver into a 12-mm-thick molybdenum base plate and then into a central 12-mm-thick ^{238}U sample surrounded by stacks of the following pairs of 10-mm-thick samples (lower sample first): Mo-Pu (δ phase), W-Pb, Al—porous Mo (19% porosity), C-LiH, Cu-Au, and Fe-quartz (crystalline). Shock-front arrival-time measurements with 80 electrical-contact pins embedded in the assembly were used to determine shock velocities with uncertainties of 1.4—2.6%; the shock front was found to be slightly curved (with a radius of curvature of ~ 2 m) but symmetric about the axis of the cylindrical driver with an upper limit on tilt asymmetry of 1.5 mrad. The measured shock velocity of 30.60 km/s in the molybdenum base plate corresponds to a pressure of 6.43 TPa based on the improved SESAME equation of state (EOS) for molybdenum. Impedance-matching analyses using the molybdenum base plate as the standard or reference material for the lower samples and using the lower samples as standards for the upper materials gave the following Hugoniot points in pressure (P) particle-velocity (u) coordinates for the indicated sample materials: Al($P=2.93$ TPa, $u=27.57$ km/s), porous Mo(4.65, 19.99), C(2.64, 28.38), LiH(1.225, 35.52), Cu(6.06, 21.15), Fe(5.71, 21.73), and quartz(2.75, 26.76). For the porous molybdenum sample, the calculated Hugoniot based on the SESAME EOS barely lies within the region of uncertainty around the measured point. For the other samples, the calculated Hugoniots are in good agreement with the measured points.

I. INTRODUCTION

For many materials, state-of-the-art equation-of-state (EOS) calculations obtained using various theoretical models and computational methods show only minor differences at the pressures attainable in conventional[1,2] laboratory experiments. However, at higher pressures the differences increase, and ultra-high-pressure EOS experiments can provide tests for distinguishing among competing theories and calculational techniques (see, for example, Refs. 2—7). In order to provide definitive tests, however, precise measurements are needed. Improved laboratory techniques[8,9] for reaching high pressures are still in the developmental stages and have not yet produced precise results. Within the last few years, nuclear-explosive-driven shock waves have been used to obtain EOS data at extremely high pressures. Soviet impedance-matching experiments[10–16] using iron for a standard have resulted in Hugoniot data for several materials at pressures of 3—12 TPa, but in some cases, the rather large experimental errors do not provide stringent tests for different EOS theories.

In two earlier nuclear-explosive-driven experiments [referred to as I (Refs. 17 and 18) and II (Refs. 19—21)], we used the impedance-matching technique[19,22] to obtain precise Hugoniot data for a single sample (in I) and 13 samples (in II). In both experiments, a strong shock (~ 5 TPa) first passed through a molybdenum base plate which served as a standard or reference material; in an earlier measurement,[23] we obtained an absolute Hugoniot point for molybdenum at 2.0 TPa, thereby providing benchmark data that helped substantiate its theoretical EOS at high pressure. Comparison of the results from experiments I and II with calculations based on the SESAME EOS library[24] indicated the need for improved theoretical treatments for several materials, namely, uranium, porous molybdenum ($\rho_0=8.29$ g cm^{-3}), amorphous quartz, and lead. Good agreement was obtained for most of the other materials. These results stimulated interest in additional high-pressure EOS data and, as an extension of these earlier measurements, we recently fielded a similar nuclear-explosive-driven experiment.

II. EXPERIMENTAL SETUP AND TECHNIQUE

The experimental configuration for the EOS package was nearly identical to that used in II and described in detail in Ref. 19. Briefly, the sample arrangement consisted of a 180-mm-diam molybdenum disk positioned on top of a uranium-lead driver with 13 samples located atop the molybdenum base plate, which again served as the standard or reference material. The samples, each approximately 50 mm across, were arranged in six stacks around a central, hexagonally shaped 12-mm-thick piece of depleted uranium (^{238}U). The outer stacks consisted of 10-mm-thick machined ingots of the following pairs of materials (with the lower one given first): Mo-Pu (δ-phase), W-Pb, Al—porous Mo (19% porosity, $\rho_0=8.24$ g cm^{-3}),

C-LiH, Cu-Au, and Fe-quartz (crystalline). The porous molybdenum was formed by hot pressing molybdenum powder to 81% of full density to obtain homogeneous samples with pore sizes less than 10 μm. Each material sample was checked for voids, imperfections, and impurities using x rays, chemical analyses, and density and sound speed measurements.

Arrival times of the shock front at 80 different positions in the sample assembly were determined by embedding electrical-contact pins[25] in the various materials. Sixteen pins were embedded in the molybdenum base plate (standard) at nominal 1-mm intervals in the vertical z direction and with a widely spaced distribution in the horizontal plane. Three pins were recessed to a depth 10 mm below the upper surface of the standard, and this depth was used as the reference "zero level" for the entire sample assembly. Four pins were inserted beyond the zero level into the lead driver, and five pins were held securely against the upper surface of the standard. Nine pins were embedded in each outer sample stack and six in the central sample, at 2-mm vertical intervals in the lower samples and at either 2- or 3-mm intervals in the upper samples. Figure 1 shows a schematic of the sample arrangement with the small circles indicating the positions of the pins, and Table I gives their x, y, and z coordinates.

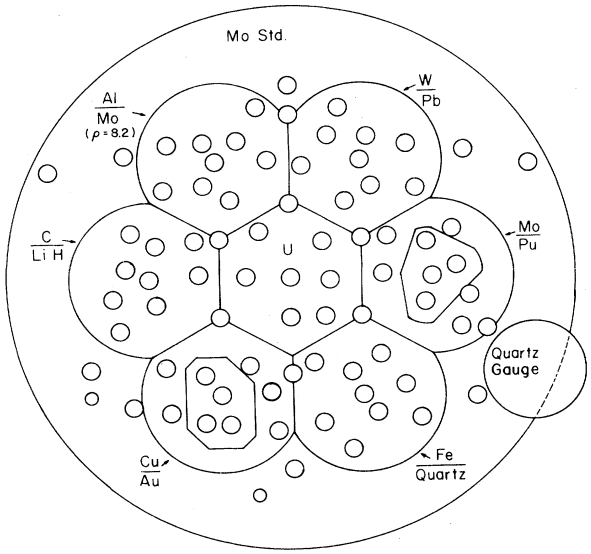

FIG. 1. Schematic showing a top view of the EOS sample package which was located about 3.5 m from the nuclear explosion. The large outer circle represents the 12-mm-thick by 180-mm-diam molybdenum base plate and the outer ring of truncated circles shows the shapes of the six stacks of 10-mm-thick samples with the labels indicating the lower-upper material in each pair; the inner hexagon shows the 12-mm-thick uranium (^{238}U) sample. The gold and plutonium samples were not truncated disks but were configured to save material without degrading their shock behavior. The small circles show the locations of the 80 electrical-contact pins with the bases of four pins terminating in the lead driver, sixteen in the molybdenum base plate, five in each lower outer sample, four in each upper sample, and six in the uranium. The position of the piezoelectric quartz gauge atop the 5-mm-thick uranium (3% ^{235}U) disk is shown at the right.

All but two pins were 4.5-mm o.d. and consisted of an aluminum center conductor inside an epoxy-filled polycarbonate (Lexan) tube that was plated with a 25-μm-thick layer of copper. The other two pins were constructed from 3.6-mm-o.d. coaxial cable with a solid copper outer shield. Both types of pins were $\sim$0.7 m long with a nominal transmission impedance of 50 Ω.

The pins were positioned so that rarefactions originating at edges would not perturb the shock front prior to its arrival at a given pin location. SESAME-based predictions indicated that the rarefaction lateral unloading angle[26] $\alpha \lesssim 32°$, and as a conservative criterion, pin positions were determined using $\alpha = 35°$ ($\tan\alpha = 0.7$). The optimum horizontal distribution was determined using a computer code that checked the horizontal distances to all rarefaction-producing edges to select the location with the greatest separation from these edges, and for almost all cases, the optimized distances exceeded the distances determined using $\tan\alpha = 0.7$ by greater than 0.3 mm.

The sample package was located $\sim$3.5 m from the nuclear explosive, and extensive shielding was used to reduce the neutron and γ-ray backgrounds, which could heat the samples and degrade the performance of the pins. Detailed Monte Carlo calculations,[27] using a complete 3D representation of the layout, indicated that the temperature rise even in the fissionable materials would be less than 100 K with the temperature rise for the other samples being less than 10 K. A piezoelectric quartz gauge[28] mounted atop a 5-mm-thick uranium (3% ^{235}U) disk was positioned near the EOS samples as shown in Fig. 1, and the pressure pulse driven into the quartz provided a measure of the energy deposition by background radiations.

III. INSTRUMENTATION AND DATA RECORDING

The center conductors of the electrical contact pins were charged to a potential of -600 V, and five pins were multiplexed onto each of 16 uphole cables. The multiplexing units for the pins used constant-impedance electrical networks with different time constants to produce pulses that return to the baseline with characteristic decay shapes, thereby providing a unique signature for each pin-closure signal. Time constants in ns of 50, 20, 30, 65, and 200 were selected on the basis of preshot predictions to give adequate recovery time between closure pulses, with the long decay time used for the last pin on a cable.

All of the signals were recorded as photographs of oscilloscope traces and each recording included a time-base trace applied $\sim$1 s before explosion time. Two sets of recordings on primary and backup oscilloscopes with different trigger systems were used to provide redundant coverage at different sweep rates. For the primary recordings, several sequentially triggered oscilloscopes formed a recording chain for each signal and covered intervals of 2–4 μs at sweep rates of $\sim$100 ns/cm. A total of 63 oscilloscopes were used to provide the necessary coverage at this sweep rate. Backup recordings were made at sweep rates of 0.25 and 1.0 μs/cm and covered intervals of either

TABLE I. Pin coordinates.

Pin number	Pin coordinate (mm)			Pin number	Pin coordinate (mm)		
	x	y	z[a]		x	y	z[a]
1	0.01	24.46	0.00	41	−27.26	30.96	25.04
2	58.05	−39.93	0.00	42	−27.30	44.71	26.96
3	−63.94	−29.75	0.01	43	−23.56	38.57	30.04
4	55.20	41.62	2.01	44	−30.32	12.81	11.99
5	−22.34	−12.70	3.03	45	−54.22	−16.76	14.02
6	0.00	53.90	4.01	46	−29.27	1.10	16.00
7	22.37	−12.69	5.00	47	−50.68	15.41	17.98
8	−52.19	40.99	6.04	48	−56.43	−6.31	20.05
9	22.36	12.71	7.01	49	−42.87	11.06	23.04
10	−50.12	−42.45	8.04	50	−42.61	−8.83	24.95
11	−22.34	12.70	9.02	51	−52.27	3.56	26.96
12	0.00	63.70	10.01	52	−44.67	0.00	30.04
13	0.00	0.00	10.01	53	−4.75	−50.78	11.98
14	0.00	−31.98	10.01	54	−40.01	−29.43	13.98
15	0.00	−63.86	10.01	55	−6.95	−37.79	16.01
16	61.87	−17.62	10.01	56	−38.40	−44.42	18.01
17	30.77	13.06	12.01	57	−13.62	−29.08	20.05
18	53.80	−16.99	13.99	58	−27.74	−47.67	23.03
19	29.22	0.99	16.01	59	−27.73	−32.25	25.02
20	51.27	15.24	18.00	60	−19.93	−48.44	27.04
21	56.27	−6.59	20.05	61	−22.33	−38.68	30.04
22	43.27	11.30	23.06	62	41.99	−46.89	12.01
23	42.51	−9.20	25.13	63	6.75	−28.20	14.00
24	52.31	3.35	27.10	64	18.85	−56.90	16.02
25	44.67	0.00	30.00	65	28.15	−25.81	18.03
26	4.05	37.10	12.00	66	9.74	−48.13	20.05
27	39.91	29.31	13.99	67	35.72	−35.92	23.02
28	15.85	56.00	15.96	68	18.94	−31.30	25.02
29	17.51	25.29	18.02	69	26.72	−45.06	26.92
30	37.22	43.73	20.03	70	22.57	−38.93	30.02
31	11.75	47.03	22.99	71	−9.82	15.40	12.01
32	26.09	30.19	24.97	72	11.14	−13.11	14.02
33	24.57	46.35	26.92	73	10.23	11.92	16.02
34	22.40	38.68	30.00	74	−13.98	0.24	18.02
35	−10.31	56.40	11.99	75	12.63	−0.81	20.03
36	−39.97	29.42	13.99	76	−0.01	−13.23	22.04
37	−6.89	39.03	15.96	77	−10.72	−71.65	−2.00
38	−38.48	44.41	17.98	78	−64.10	−38.97	−6.12
39	−18.86	26.11	20.04	79	75.61	35.89	−19.50
40	−16.62	45.44	23.03	80	−75.54	35.84	−19.50

[a]Distance from the zero-level in the molybdenum base plate (see text and Fig. 1 for definition).

5 or 10 μs, respectively, with the 10-μs recordings used for the quartz gauge.

Two trigger systems were used for the primary recordings with the early time oscilloscopes triggered by a delayed explosion-produced γ-ray signal, and subsequent oscilloscopes were triggered by the first pin pulse. Backup triggers were derived from the command signal that initiated the explosion.

For all the fast-sweep oscilloscopes using a common trigger pulse, different time intervals were covered by displacing the initial horizontal position of the beam. The trigger pulse generated a series of time-tie (TT) pulses ~ 1 ns wide that were applied to a separate set of oscilloscope deflection plates and appeared as a sharp spike superimposed near one end of each fast-sweep signal trace. A series of common-timing (CT) calibration recordings were made to relate the time on one trace to that on another by simultaneously applying a sequence of timing pulses to all signal lines. Uncertainties in the intervals from the TT pulses to the CT pulses varied from 0.5 to 2.5 ns and were caused mainly by the relatively slow rise times of the CT pulses.

The time base for the fast-sweep oscilloscopes was a nominal 100-MHz sine wave produced by a high-power pulsed oscillator. The oscillator frequency was found to vary slightly along the output train, and a temperature-

controlled crystal oscillator was used as a calibration standard to determine a correction for each recording interval; the maximum correction to a measured interval was 3 ns.

IV. EXPERIMENTAL RESULTS

Figure 2 shows a representative photographic film record for one of the sequentially triggered fast-sweep oscilloscopes. The lower sweep is the signal trace and shows four fast-rise closure pulses indicating shock arrival at the pins labeled 9, 36, 48, and 41 in Table I; the sharp spike near the left end is the time-tie pulse used for common timing. The upper sweep is the time base with a 10-ns period.

All 80 pins produced signals of this quality on the fast-sweep oscilloscope records from which each TT to closure-pulse interval was determined with an accuracy of ± 1 ns. Measurements of this interval were carried out using both a 70-power film reader with a crosshair marker connected to a digital readout and a set of enlarged photographic prints of the film negatives; the results from the two methods agreed to within about 1 ns. The measured intervals were corrected using the common-timing data, the measured cable lengths, and the calculated Lexan-plug closure-time differences (due to plug-thickness and sample-impedance variations) to determine the relative closure times for all 80 pins with an overall uncertainty for each time of ~ 3 ns. These corrected relative closure times are given in Table II for the pertinent pins from Table I.

The observed signal from the quartz gauge exhibited a 1.7-μs-wide pulse whose amplitude varied smoothly from 0.5 to 1.5 V. This duration corresponds to the expected transit time of a pressure pulse through the gauge; at later times the unloading wave and noise induced by background radiation combined to produce an erratic output signal. The observed signal level implied an initial pressure in the uranium between 0.23 and 0.35 GPa based on the SESAME EOS tables for uranium and quartz and assuming instantaneous energy deposition; the corresponding temperature rise in the enriched uranium was 65 ± 15 K with an implied temperature rise of less than 10 K for the nonfissioning samples—in very good agreement with Monte Carlo predictions.

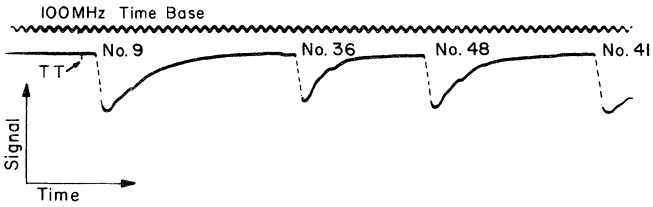

FIG. 2. Representative photographic record from one oscilloscope showing both the 100-MHz time base (upper) and a portion of the signal from one cable (lower). The signal trace exhibits four closure pulses with rise times of ~ 5 ns that indicate shock arrival at the bases of pins labeled 9, 36, 48, and 41 in Tables I and II. The rises were clearly visible in the originals but are enhanced in this reproduction with dashed lines. The sharp spike (~ 1 ns wide) near the start of this sweep is the time-tie (TT) pulse; similar spikes appeared on all records and provided cross-timing information for interrelating the oscilloscope signals. All 80 pins produced pulses of this quality with little, if any, pileup induced distortions. Shock-arrival times were determined relative to the TT on a given trace with an accuracy of ± 1 ns, but the cross-timing corrections introduced uncertainties in the relative closure times for pulses on different oscilloscopes that were as large as 3 ns.

TABLE II. Pin closure times.[a]

Pin number	Closure time (ns)	Pin number	Closure time (ns)	Pin number	Closure time (ns)
1	−215.70	19	293.45	50	450.57
2	−207.66	20	381.52	51	494.34
3	−207.71	21	452.64	52	563.12
4	−137.37	35	163.44	53	177.36
5	−128.79	36	220.28	54	236.45
6	−75.42	37	263.25	55	292.46
7	−55.87	38	320.97	56	377.05
8	−5.01	39	354.64	57	419.41
9	10.35	40	478.72	62	186.06
10	61.93	41	546.49	63	220.00
11	58.01	42	620.08	64	305.09
12	127.39	43	731.37	65	347.07
13	77.06	44	144.40	66	420.44
14	101.12	45	219.54	67	485.47
15	127.54	46	245.43	68	539.62
16	125.69	47	306.16	69	599.97
17	162.30	48	363.74	70	676.70
18	246.66	49	415.81	77	−266.46

[a]Relative times measured from reference time-tie pulse.

V. DATA ANALYSIS

In a preliminary analysis, the closure times for the pins in the individual materials were plotted as a function of the z coordinates. For the molybdenum base plate, the interior pins near the central sample closed before the corresponding pins located at larger radii near the outside edges of the sample stacks. For the small samples, the closure times were also found to be correlated with the distance of a pin from the central axis of the assembly. These results indicated that the shock front was not flat; but the departure from planarity seemed to be symmetric about the central axis and implied a radius of curvature for the shock front of about 2 m. The plots also indicated that shock-decay effects were minimal and that none of the pins behaved erratically.

The corrected closure times (t) and pin coordinates (x,y,z) were then used as input variables in a least-squares fitting program to determine the shape and position of the shock front as a function of time. Different analytic functions for $t=t(x,y,z)$ were used to parametrize the closure times in terms of the coordinates, and the resulting coefficients and associated uncertainties were used to determine the shape of the front and the shock velocities. Different functional forms and subsets of pins were used, and in most cases, the fitting function was assumed to be symmetric about the vertical axis of the standard with the radial dependence given by

$$f(r)=r^2\equiv(x^2+y^2)$$

or by $f(r)=r$. The closure times for the pins in sample i were then determined from the relation

$$t_i=A_i+(B_i+C_iz)f(r)+D_iz\ . \tag{1}$$

At an interface between two materials the coefficients were allowed to change, but in such a way that the calculated times were the same at a given value of r. This requirement placed restrictions on the coefficients and was used in conjunction with other constraints to limit the number of free parameters. One such constraint resulted from considering the change in the angle of incidence (θ) for a shock crossing an interface between materials i and j. In analogy with light refraction and for shock velocities Δ_i and Δ_j,

$$\sin\Theta_j=\sin\Theta_i(\Delta_j/\Delta_i)\ ,$$

and using $\Delta_i=(dt_i/dz)^{-1}$ gives

$$\sin\Theta_i\approx\Delta_i(dt_i/dr)\ ,$$

which implies that the coefficients B_i and C_i in Eq. (1) remain unchanged on the two sides of the interface. This restriction combined with the interface-imposed restriction on A_i means that the only additional parameter needed in the fitting function for each material (after the first one) is D_i, with the subscripts on the other coefficients eliminated. This parameter D_i is closely related to the shock velocity

$$\Delta_i=[D_i+Cf(r)]^{-1}\ ;$$

the coefficient C indicates the amount of radial variation in the shock velocity, and B is related to the radius of curvature of the shock front. These and similar constraints were used to reduce the number of free parameters when other functional forms were used. The values of C determined from the fits indicated that the shock velocity varied by less than 1% from the inside to the outside of a small sample, and the values for B corresponded to a radius of curvature of $\sim$2 m.

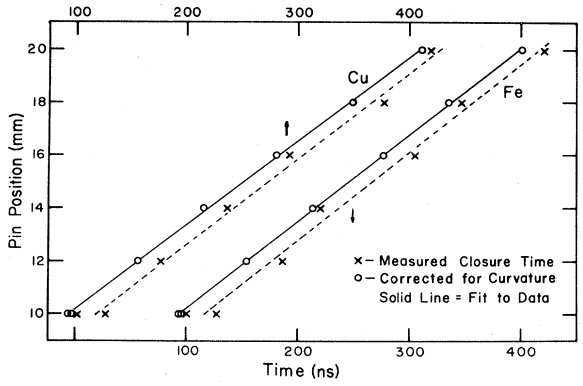

FIG. 3. Plots of closure times (abscissa) as a function of the vertical z coordinates for those pins embedded in the copper and iron samples (labeled 53—57 and 62—66 in Tables I and II); the pins at the 10-mm position terminated on the upper surface of the molybdenum base plate. The crosses ($\times$) show the measured closure times given in Table II, and the dashed straight lines are drawn to guide the eye. The open circles show the closure times after correction for curvature-related delay of shock-front arrival; the solid curves are the results of least-squares fits using a function without an r or z dependence for the shock velocity. The curvature coefficient was determined from a fit to the data for all the pins except those near the central axis is both the molybdenum base plate and the uranium.

Other functional forms with different constraints were then used along with various subsets of the pins to study possible asymmetries and shock-decay effects. Terms linear in x and y were added to Eq. (1), and these fits implied an upper limit of 1.5 mrad on the tilt angle for the axis of the curved shock front. Additional fits of a tilted plane ($B\equiv C\equiv 0$) to the pin data for each sample stack indicated that the shock front at each sample position was tangent to an axially symmetric, spherically shaped front with a radius of curvature of $\sim$2 m.

The effect of the curvature on the quality of the fit is illustrated in Fig. 3, which shows plots of the closure times as a function of the z coordinates for the pins in the copper and iron samples, with the crosses indicating the experimental results. The curvature coefficient, determined from a global fit, was used to calculate the delay in closure of each pin due to its radial position. The corrected times are shown as open circles in Fig. 3, and the solid curves are the result of least-squares fits using the function of Eq. (1) with $C_i\equiv 0$, which implies a shock velocity that is not changing with r. The dashed straight lines are drawn to guide the eye, and the scatter of the crosses about these lines is obviously greater than for the circles about the solid lines. In addition, effects associated with a

decrease in the shock velocity with propagation distance are not evident in this plot.

Shock-decay effects were studied by adding a term in z^2 to a modified version of the function in Eq. (1). These fits indicated that the shock velocity was constant through the molybdenum base plate but was decreasing by a few percent as the shock propagated through the other samples; however, the uncertainties in the velocity-decrease coefficients ranged from 30% to 70%. Additional fits were then performed with these coefficients held fixed at various values in the range determined from the previous unconstrained fits, and the smallest value of chi squared was used to select the best fit. These fits gave lower values of chi squared and much smaller uncertainties for the derived shock velocities. The resulting value of the standard deviation in each closure time was about ± 3.5 ns; this implied a value of chi squared near 1.0 and indicated that the fitting function provided a reasonably accurate representation of the motion of the shock front.

For the best fits, the resulting statistical errors in the shock velocities ranged from 0.7% to 2.3%, and when different functions or different values of the velocity-change coefficients were used in the fits, the shock velocities varied by about 1%. These variations along with the statistical uncertainties were used to assign overall experimental errors of 1.4% to 2.6% to the derived shock velocities. The final values of the shock velocities and associated errors are summarized in Table III.

VI. IMPEDANCE-MATCHING RESULTS

The derived interface shock velocities in Table III were used in performing impedance-matching analyses[19,22] for each possible pair of materials; the lower material in a pair served as the reference material (standard) with its EOS determined from theoretical calculations. Hugoniot data were determined for each lower-layer sample relative to the molybdenum base plate and for each upper-layer sample relative to the adjacent lower-level material. The combined experimental uncertainties in the two shock velocities were used to determine the overall error for each derived Hugoniot point.

Initial impedance-matching analyses were performed using early versions of the SESAME EOS tables, and the results were in reasonable agreement with experiment for many materials—but they also included some rather large inconsistencies. Therefore, for some materials other EOS tables,[4,5,29–31] based on more recent improved theoretical treatments, were converted to the SESAME format, and these were used in impedance-matching analyses. In all cases the improved theories gave better agreement with the measurements, with the changes in the calculated Hugoniots ranging from slight variations to major shifts.

A graphical analysis was performed to determine each Hugoniot point and the associated uncertainties; each graph consisted of plots in the pressure—particle-velocity (P-u) plane of the experimentally determined Rayleigh

TABLE III. Comparison of measured and calculated shock velocities.

Material	Initial density ($g\,cm^{-3}$)	Shock velocity (km/s) Measured[a] Bottom	Top	Error[b] (%)	Calculated[c] Old[e]	New[f]	Differenced[d] (%) Old[e]	New[f]
Mo Std	10.22		30.60	1.4				
Mo	10.22	30.64	29.49	1.4				
Al	2.700	39.41	38.25	1.6	39.10	39.16	−0.79	−0.63
Mo[g]	8.240	28.21		1.7	28.95	28.84	2.62	2.23
C	2.235	41.68	40.51	1.7	42.00		0.78	
LiH	0.700	49.27		2.6	49.59		0.66	
Cu	8.935	32.10	30.94	1.4	31.25	31.81	−2.64	−0.89
Fe	7.85	33.47	32.31	1.4	32.19	33.64	−3.82	0.51
Quartz	2.645	38.87		2.4	40.12	38.70	3.23	−0.43

[a]Shock velocities at lower and upper surfaces derived from least-squares fits.

[b]Overall uncertainties in percent in the measured shock velocities (see text).

[c]The shock velocity was calculated for each test sample in an impedance-matching pair using the measured interface shock velocity for the adjacent driving standard and the theoretical EOS's of both the standard and the sample materials; this technique was applied to both the molybdenum-standard and lower-level sample pairs and to the lower-level and upper-level pairs.

[d]Diffferences in percent between the calculated and measured shock velocities [equal to $100\times(\Delta_{calc}/\Delta_{expt}-1)$].

[e]Based on the SESAME EOS tables (Ref. 24) for the following material numbers: Mo (2981), Al (3710), C (7831), LiH (7370), Cu (3330), Fe (2140), and quartz (7380).

[f]Based on an improved theoretical treatment of the EOS, which was used for only one material in a pair; these materials along with their SESAME material numbers (where appropriate) were Al (3712), Cu (3331), and Fe.

[g]Low initial density.

line ($P=\rho_0\Delta u$) for the upper material and its intersection with the calculated release isentrope (RI) or reflected shock (RS) Hugoniot for the lower standard material whose initial state was defined by its measured interface shock velocity. Similar plots using shock velocities that differed by one standard deviation for both materials defined a region of uncertainty or error box for P and u, and a plot on this graph of the calculated Hugoniot for the upper material indicated whether its theoretical EOS gave agreement with the measurement. This comparison provided a check on the consistency and reliability of the theoretical treatments used for the two materials.

The analysis technique is illustrated for each sample in the graphs of Figs. 4—7. These graphs are plotted on expanded scales to illustrate the analysis details and show only the regions of interest around the measure points.

Table IV gives the experimentally determined Hugoniot data for the pertinent materials in terms of a P-u Hugoniot point and the corresponding compression $\eta\equiv\rho/\rho_0=\Delta/(\Delta-u)$ for each sample. The interface shock velocities are listed in the second column with the experimental uncertainties in the next column; the derived values for P, u, and η and their associated uncertainties are given in the next three pairs of columns. The uncertainties in η, σ_η, were calculated from the relation

$$\sigma_\eta/\eta=(\eta-1)\left[\left[\frac{\Delta}{u}\frac{\partial u}{\partial\Delta}-1\right]^2\left[\frac{\sigma_\Delta}{\Delta}\right]^2+\left[\frac{D}{u}\frac{\partial u}{\partial D}\right]^2\left[\frac{\sigma_D}{D}\right]^2\right]^{1/2},$$

where Δ and D are the measured shock velocities in the sample and reference materials, respectively, and the σ's correspond to one standard deviation in the velocities; the partial derivatives were evaluated numerically using the analysis plots in Figs. 4—7.

For the case in which a material was treated as a standard without subsequently serving as an upper-level sample, the Hugoniot data in Table IV were derived from its theoretical EOS using the measured shock velocity and its associated uncertainty. The values given for the molybdenum base plate (three cases) were obtained in this manner, and the results reflect how well a shock velocity measurement defines a Hugoniot point for a material whose EOS is known. In this cases, the small errors in η reflect the correlation between Δ and u on the Hugoniot and were calculated using $\sigma_D\equiv 0$.

The details of the analysis and the results for each material are discussed below with references made to the summaries in Table III and IV and to the plots in Figs. 4—7. In these plots, the calculated Hugoniots based on the most recent theoretical predictions are shown as heavy solid curves with dashed heavy curves showing the Hugoniots based on older theories.

Molybdenum base plate

For the cases in which the data for only the exterior molybdenum pins and sample stacks were included in the fits, the resulting outer-radius shock velocity at the upper surface of the base plate was $\approx$29.8 km/s. From these same fits, however, the derived velocity at the lower surface of the small molybdenum sample was slightly greater than 30.6 km/s. These fits included a z^2 term in the fitting function with the $f(r)$ coefficient $C\equiv 0$, but other fits

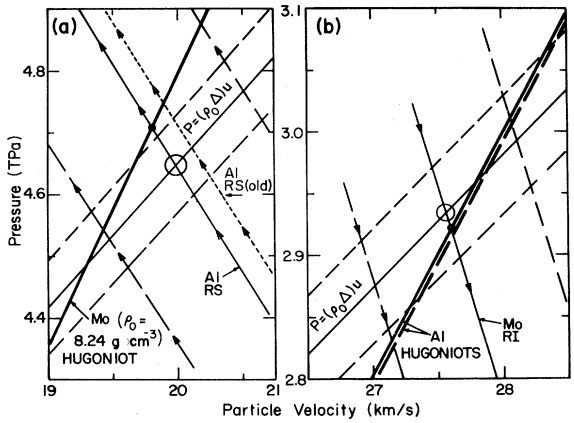

FIG. 4. Plots in the P-u plane illustrating the graphical method for determining Hugoniot points for (a) porous molybdenum ($\rho_0=8.24$ g cm^{-3}) and (b) aluminum from impedance-matching analyses. The experimentally determined point for aluminum (circled) occurs at the intersection of the release isentrope (RI, denoted by arrows, $\rightarrow$) from the initial shock state in the molybdenum ($\Delta=30.60$ km/s) with the Rayleigh line ($P=\rho_0\Delta u$) for aluminum corresponding to an experimental shock velocity of 39.41 km/s. The heavy curves show the aluminum Hugoniots calculated using the SESAME EOS tables for the original (dashed curve, material number 3710) and improved (solid curve, material number 3712) theoretical treatments. The intersections of the molybdenum RI with these curves occur slightly below the measured point and correspond to shock velocities that differ by less than 1% from the experimental value; the intersection with the improved EOS at the point indicated by the large dot (●) gives slightly better agreement. The lighter dashed curves on either side of both the molybdenum RI and the aluminum Rayleigh line show the variations in these curves implied by the experimental errors in the two shock velocities quoted in Table III, and the area bound by their intersections corresponds to the region of uncertainty for the derived point. The derived Hugoniot point [circled in (a)] for the porous-molybdenum sample corresponds to the intersection of its experimentally determined Rayleigh line ($\Delta=28.21$ km/s) with the aluminum reflected shock (RS) Hugoniot, which is based on the improved SESAME EOS and the measured upper-surface shock velocity of 38.25 km/s; the intersection point for the RS Hugoniot that is based on the original SESAME EOS and shown as a curve of small dashes lies somewhat higher. The dashed curves, which correspond to the experimental errors in the shock velocities, form a box indicating the region of uncertainty for both P and u. The calculated molybdenum Hugoniot (heavy curve) based on its SESAME EOS (material number 2981) for an initial density of 8.24 g cm^{-3} lies well above this point, but within the error box, and intersect the aluminum RS Hugoniot at the point indicated by the large dot (●).

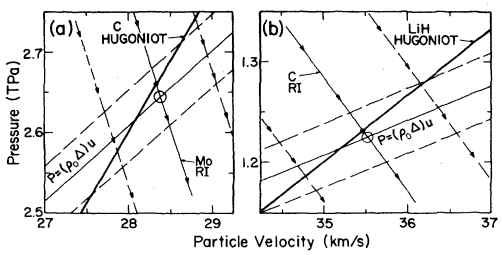

FIG. 5. Plots in the P-u plane comparing the theoretical Hugoniots (heavy curves) with the experimentally determined points (circled) for the materials in the C-LiH stack (see Fig. 4 for notation). In (a) the RI from the initial state in the molybdenum ($\Delta=30.60$ km/s) intersects the carbon Rayleigh line, determined from the measured lower-surface shock velocity of 41.68 km/s, at a point almost coincident with the one predicted by the SESAME EOS for carbon (material number 7831) and indicated by the large dot (●). The dashed curves indicate the variations in the molybdenum RI and the carbon Rayleigh line arising from the experimental errors in the shock velocities and define a region of uncertainty around the measured point. The experimentally determined point for LiH (b) occurs at the intersection of the carbon RI from its initial state defined by $\Delta=40.51$ km/s with the LiH Rayleigh line determined from the measured lower-surface shock velocity of 49.27 km/s for this sample. This point for LiH is also almost coincident with the one predicted by its SESAME EOS (material number 7370), and the corresponding Hugoniot passes almost through the center of the region of uncertainty, which is bound by the dashed curves corresponding to the experimental errors in the shock velocities for both carbon and LiH.

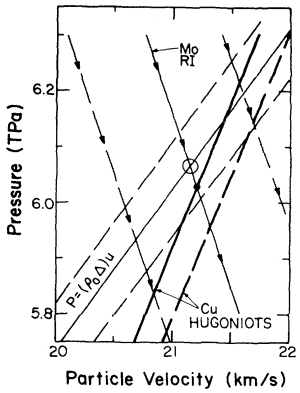

FIG. 6. Plots in the P-u plane comparing the theoretical Hugoniots for copper with the experimentally determined points for this material (see Fig. 4 for notation). The RI from the initial state in the molybdenum ($\Delta=30.60$ km/s) intersects the copper Rayleigh line ($\Delta=32.10$ km/s) to define a Hugoniot point for copper indicated by the open circle. The region bound by the dashed curves indicates the uncertainties in P and u corresponding to the experimental errors in the shock velocities given in Table III for the molybdenum standard and the copper sample. The calculated Hugoniot based on the original SESAME EOS for copper (material number 3330) is shown as the heavy dashed curve that barely passes through the corner of the error box; however, the calculated Hugoniot that is based on the improved EOS (material number 3331) and shown as the heavy solid curve intersects the molybdenum RI at the point indicated by the large dot (●) and passes much closer to the measured point.

with the $Czf(r)$ term not set to zero implied a slight change in the velocity with radius and were consistent with a larger velocity of 30.60 km/s at the upper surface of the molybdenum base plate at a radial distance corresponding to the positions of the outer small samples. This value of Δ, given in the first line of both Tables III and IV, was used to determine the initial shock state of the molybdenum for the impedance-matching analyses with the adjacent outer samples. The pressure at this value of Δ, based on the SESAME EOS (material number 2981), is 6.434 TPa$\pm$3.15% and corresponds to compression by a factor of 3.05$\pm$0.7%.

Similar fits that included only pins nearer the axis resulted in a slightly larger shock velocity. These fits, which used the data for the interior molybdenum pins and for those in the uranium, gave an upper-surface shock velocity in the molybdenum of 31.00 km/s. This velocity was consistent with the outer shock velocity and the value of the C coefficient that were determined from previous fits, and the curvature coefficient (B) indicated a slightly smaller radius of curvature over the interior region of the shock front.

The lower-surface shock velocity in the molybdenum base plate at large radial distances corresponding to the positions of the pins in the lead driver was found to be 30.40 km/s. This value, based on fits to pin data for the driver and the outer portion of the molybdenum, was consistent with previous results, which had indicated that the molybdenum shock velocity was not changing with propagation distance but was slightly less at larger radii. The shock velocities of 31.00 km/s and 30.40 km/s were used with the SESAME EOS library to calculate the Hugoniot points given in the lower part of Table IV.

Molybdenum sample

As mentioned previously, the derived shock velocity of $\sim$30.6 km/s at the lower surface of the small molybdenum sample helped determine the upper-surface shock velocity in the molybdenum base plate at the outer-stack positions. The corresponding upper-surface velocity of 29.49 km/s for this small sample defined the initial state for the reflected shock produced at the plutonium interface, and Table IV gives the resulting SESAME-based Hugoniot point for this shock velocity.

Aluminum-porous molybdenum ($\rho_0=8.24$ g cm^{-3}) stack (Fig. 4)

The predicted shock velocities in aluminium based on both the old and new[31] SESAME EOS tables (material numbers 3710 and 3712, respectively) are in excellent agreement with the measured point, with the new EOS giving slightly better agreement. As seen in Fig. 4(b), the Hugoniot for the new EOS is only slightly stiffer than the

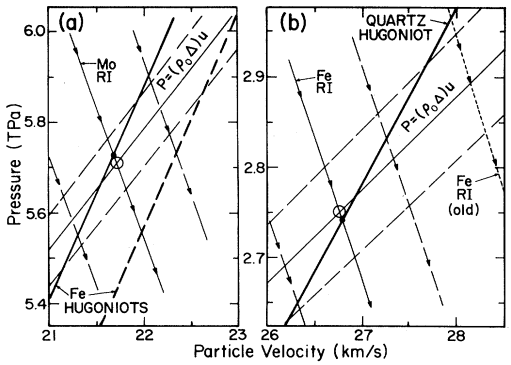

FIG. 7. Plots in the P-u plane comparing the theoretical Hugoniots for iron (a) and crystalline quartz (b) with the experimentally determined points for this pair of materials (see Fig. 4 for notation). The measured point for iron occurs at the intersection (circled) of the molybdenum RI from its initial shocked state (defined by $\Delta=30.60$ km/s) with the Rayleigh line for iron corresponding to a lower-surface shock velocity of 33.47 km/s. The lighter dashed curves show the variations implied by the experimental shock-velocity errors given in Table III, and the bound region indicates the uncertainties associated with the measured point. The calculated iron Hugoniot based on the original SESAME EOS (material number 2140) is the heavy dashed curve that lies well below the measured point and does not pass through the error box; the Hugoniot, based on the improved theoretical treatment of the iron EOS and shown as the heavy solid curve, intersects the molybdenum RI at the point indicated by the large dot (●) and lies well within the region of uncertainty. The derived Hugoniot point for quartz (circled) occurs at the intersection of the iron RI, calculated using the improved EOS for an initial state defined by the measured upper-surface shock velocity of 32.31 km/s, with the experimentally determined Rayleigh line for quartz ($\Delta=38.87$ km/s). The Hugoniot point predicted by the SESAME EOS for quartz (material number 7380) is indicated by the large dot (●) at the intersection of the iron RI with the calculated quartz Hugoniot, which is shown as a heavy curve. The lighter dashed curves show the variations in the iron RI and the quartz Rayleigh line that are implied by the experimental errors in the shock velocities; the region bound by the intersections of these dashed curves indicates the uncertainties in P and u. The iron RI based on the original SESAME EOS is shown as a curve of small dashes and intersects the quartz Rayleigh line well below the predicted point, which occurs at the intersection of the RI with the calculated quartz Hugoniot. However, the corresponding region of uncertainty (not shown) around this experimental point based on the original iron EOS overlaps the quartz Hugoniot slightly.

old one, but the change moves the new Hugoniot toward the experimental point. Both RS Hugoniots, based on the upper-surface shock velocity in the aluminum, intersect [Fig. 4(a)] the experimentally determined Rayleigh line ($P=\rho_0\Delta u$) for the porous molybdenum at pressures almost 0.07 TPa below those predicted by the SESAME EOS for molybdenum at an initial density of 8.24 g cm^{-3}. The differences, however, are within the experimental uncertainties with the new EOS for aluminum again giving better agreement with the experiment. These results indicate that the Hugoniot for the porous molybdenum could be softer; this implied change is much smaller than, but in the same direction as, that indicated by the results[19] of experiment II.

Carbon-LiH stack (Fig. 5)

The shock velocities predicted by the SESAME EOS tables for both carbon and LiH (material numbers 7831 and 7370, respectively) differ from the measured values by less than 1%. The EOS table for carbon was generated[32] during the design stage of this experiment to provide better predictions than those based on an older EOS for diamond (material number 7830); this older EOS implied a Hugoniot curve (not shown) that barely intersected the error box and a shock velocity more than 3% below the measured value. The experimental uncertainty in the LiH shock velocity is considerably larger than for most other samples and reflects the somewhat larger amount of scatter in the closure-time data. This scatter is probably caused by several lower-surface imperfections in this soft material that were noted at assembly time. When the data for the pins near these indentations are excluded from the fits, the resulting velocity does not change appreciably, but the corresponding errors increase significantly because of the reduced number of data points.

Copper sample (Fig. 6)

The predicted shock velocity in copper based on the original SESAME EOS (material number 3330) is lower than the measured value by nearly 3% and lies within the limits imposed by the experimental errors by only 0.2% (see Fig. 6). Predictions based on the improved[4,5] EOS for copper (SESAME material number 3331) differ from the measured value by less than 1%.

Iron-quartz stack (Fig. 7)

The RI from the initial state in the molybdenum standard intersects the experimentally determined Rayleigh line for iron at a pressure ~3% higher than that predicted by its SESAME EOS (material number 2140), and the corresponding Hugoniot lies outside the region of uncertainty defined by the shock-velocity errors. With this EOS for iron, the resulting impedance-matching Hugoniot point for quartz lies well below the point predicted by the SESAME EOS for quartz (material number 7380). However, the rather large uncertainty of 2.4% in the quartz shock velocity results in an error box (not shown) that overlaps the calculated quartz Hugoniot, but a reduction of this uncertainty by only 0.6% would eliminate this overlap. These results indicated that the iron Hugoniot needs to be considerably stiffer and that the quartz Hugoniot could be somewhat softer; both discrepancies prompted further investigation for this pair.

An existing[29,30] EOS for iron, based on an improved theoretical treatment,[33,34] was converted to the SESAME format and used in an impedance-matching analysis. The Hugoniot point predicted by the improved EOS lies less than 0.02 TPa (or 0.35%) above the experimental point and corresponds to a shock velocity only 0.5% greater

TABLE IV. Measured Hugoniot points.

Material	Measured Shock velocity[b] (Δ) (km/s)	Error (%)	Derived Hugoniot parameters[a] Pressure[c] (TPa)	Error[d] (%)	Particle velocity[c] (u) (km/s)	Error[d] (%)	Compression[c] $\left[\eta \equiv \frac{\Delta}{\Delta - u}\right]$	Error[d,e] (%)
Mo Std	30.60†	1.4	6.434	3.15	20.57	1.75	3.05	0.7
Mo	29.49†	1.4	5.918	3.17	19.64	1.78	2.99	0.8
Al	39.41	1.7	2.933	3.26	27.57	2.18	3.33	5.4
Mo[f]	28.21	1.7	4.647	3.59	19.99	3.30	3.43	6.7
			4.676*[a]	3.58*[d]	20.12*	3.28*	3.49*	6.9*
C	41.68	1.7	2.644	3.31	28.38	2.35	3.13	5.1
LiH	49.27	2.6	1.225	4.38	35.52	2.96	3.58	8.0
Cu	32.10	1.4	6.065	3.12	21.15	2.62	2.93	4.6
Fe	33.47	1.4	5.709	3.14	21.73	2.60	2.85	4.4
Quartz	38.87	2.4	2.752	3.96	26.76	2.77	3.21	6.2
			2.894*[a]	3.85*[d]	28.16*	2.56*	3.63*	7.1*
Mo Std[g]	31.00†	1.6	6.625	3.59	20.91	2.00	3.07	0.8
Mo Std[h]	30.40†	1.4	6.342	3.21	20.41	1.81	3.04	0.8

[a]When appropriate, the derived values are based on an improved theoretical treatment of the EOS of the driving standard; the values flagged with an asterisk (*) are based on the original SESAME EOS tables. See Table III for the SESAME material numbers.
[b]Measured shock velocities at the lower interfaces, except for those flagged with a dagger (†); the flagged values were used with the SESAME EOS library to determine the tabulated Hugonoit parameters which defined the initial state when the material was used as the driving standard (see c below).
[c]Hugoniot data derived from the graphical analyses shown in Figs. 4–7, except for the cases in which the shock velocity is flagged with a dagger (†) and the material was treated as the standard with the Hugoniot parameters determined from the theoretical EOS.
[d]Determined from the uncertainties in the shock velocities and do not include uncertainties associated with the EOS of the standard; for a dagger-flagged shock velocity, the corresponding experimental error alone was used to determine the quoted errors in the Hugoniot parameters from the theoretical EOS.
[e]Calculated using the error propagation expression in the text with the values of the dagger-flagged shock velocities reflecting the high correlation between Δ and u on the Hugoniot.
[f]Low initial density, $\rho_0 = 8.24\ \mathrm{g\,cm^{-3}}$.
[g]Near the central axis (see text).
[h]Near the outer diameter (see text).

than the measured value. When the improved EOS is used, the calculated RI from the experimentally determined initial state in iron intersects the measured Rayleigh line for quartz within 0.01 TPa of the pressure calculated using the SESAME EOS for quartz. Thus, this existing improved EOS for iron eliminates the discrepancies noted earlier and gives better agreement with the experimental results for both materials.

VII. SUMMARY

This experiment provides rather precise Hugoniot data for many materials at pressures nearly ten times as high as those reached in conventional laboratory experiments, and the resulting densities correspond to threefold compressions. These data along with those from earlier similar measurements provide benchmarks for testing various theories in a pressure region where sizable differences can occur between predictions based on different models. While these relative measurements rely on the knowledge of the EOS of a standard material in each case, the results allow the consistency of the models to be tested.

In general, results obtained using the SESAME EOS library[24] are in reasonably good agreement with the experimentally determined Hugoniot points for many of the sample materials, especially when the EOS tables are based on improved[33–35] theoretical calculations. However, for the materials with low-initial or less-than-crystalline densities, predictions of shock velocities consistently show larger-than-average differences from the measured values. This statement includes the discrepancies noted for the porous molybdenum sample in the present experiment and in experiment II, as well as for the quartz sample in experiment II. In these cases, the SESAME-based predictions of the shock velocities in the low-density materials are too high, implying that the Hugoniots for thse materials need to be softer. Hopefully, these results will stimulate additional improved theoretical

calculations and the development of more sophisticated EOS models, which can be meaningful tested against these benchmark measurements to provide added insight into the physics at these extreme conditions.

ACKNOWLEDGMENTS

Many people contributed to the overall success of this experiment, and without their support, it would have been impossible to meet the rigid schedule imposed by its very nature. In particular, the personnel in the Test Engineering Group aided considerably by their cooperative interaction in designing the overall downhole-rack configuration, and their field-support members headed by R. Sharp provided continuous material and manpower support during the installation of the apparatus. B. C. Diven contributed invaluable advice and information based on his general knowledge and experience in areas related to such experiments. I wish to especially thank the other members of the Nuclear Physics Group for their conscientious support during all phases of the design, mechanical and electrical assembly, and data recording for this experiment; this team included W. A. Teasdale, E. E. Robinson, J. M. Anaya, M. A. Osborn, and Q. Jones. Outstanding data recording based on extensive experience was provided by J. E. Allen of the Fast Transient Measurement Group and R. Schiltz and other EG&G support personnel. In addition, calculational support was provided by members of the Applied Theoretical Physics Division with help coming specifically from M. Rich and R. B. Schultz of the Diagnostics Physics and the Thermonuclear Applications Groups. G. I. Kerley of the Computational Physics Group along with J. Shaner of the Shock Wave Physics Group and members of the Theoretical Division, Equation-of-State and Opacity Group contributed information and advice related to the selection of the sample materials to be used; additional sample-selection advice from H-Division personnel at Lawrence Livermore National Laboratory was coordinated by W. J. Nellis of that division. And finally, I would like to thank M. Rich and B. C. Diven for their helpful comments and suggestions after reading a draft of this manuscript. This work was performed under the auspices of the U.S. Department of Energy.

[1]R. G. McQueen, S. P. Marsh, J. W. Taylor, J. N. Fritz, and W. J. Carter, in *High-Velocity Impact Phenomena,* edited by R. Kinslow (Academic, New York, 1970), p. 293 and references therein.

[2]Lee Davison and R. A. Graham, Phys. Rep. 55, 255 (1979) and references therein.

[3]H. Graboske and L. Wong, Lawrence Livermore Laboratory report UCRL-52323, pp. 19–22 (unpublished).

[4]K. S. Long, D. Young, and F. H. Ree, in *Shock Waves in Condensed Matter—1981 (Menlo Park),* Proceedings of the Conference on Shock Waves in Condensed Matter, AIP Conf. Proc. No. 78, edited by W. J. Nellis, L. Seaman, and R. A. Graham (AIP, New York, 1982), pp. 213–217.

[5]K. S. Trainor, J. Appl. Phys. 54, 2372 (1983).

[6]G. I. Kerley and P. M. Henry, Los Alamos Science Laboratory report LA-8062 (unpublished).

[7]B. I. Bennett and G. I. Kerley (private communication).

[8]See, for example, Sec. XI on "Dynamic Pressures—Experimental Techniques," in *High Pressure Science and Technology,* edited by B. Vodar and Ph. Marteau (Pergamon, New York, 1980), Vol. 2, pp. 958–1008.

[9]See Ref. 4, Chap. III, p. 145.

[10]L. V. Al'tshuller, B. N. Moiseev, L. V. Popov, G. V. Simakov, and R. T. Trunin, Zh. Eksp. Teor. Fiz. 54, 785 (1968) [Sov. Phys.—JETP 27, 420 (1968)].

[11]R. F. Trunin, M. A. Podurets, B. N. Moiseev, G. V. Simakov, and L. V. Popov, Zh. Eksp. Teor. Fiz. 56, 1172 (1969) [Sov. Phys. JETP—29, 630 (1969)].

[12]M. A. Podurets, G. V. Simakov, R. F. Trunin, L. V. Popov, and B. N. Moiseev, Zh. Eksp. Teor. Fiz. 62, 710 (1972) [Sov. Phys.—JETP 35, 375 (1972)].

[13]R. F. Trunin, M. A. Podurets, G. V. Simakov, L. V. Popov, and B. N. Moiseev, Zh. Eksp. Teor. Fiz. 62, 1043 (1972) [Sov. Phys.—JETP 35, 550 (1972)].

[14]E. N. Avrorin, B. K. Vodolaga, L. P. Volkov, A. S. Vladimirov, V. A. Simonenko, and B. T. Chernovolyuk, Zh. Eksp. Teor. Fiz. Pis'ma Red. 31, 727 (1980) [Sov. Phys.—JETP Lett. 31, 685 (1980)].

[15]L. P. Volkov, N. P. Voloshin, R. A. Mangasarov, V. A. Simonenko, G. V. Sin'ko, and V. L. Sorokin, Zh. Eksp. Teor. Fiz. Pis'ma Red. 31, 546 (1980) [Sov. Phys.—JETP Lett. 31, 513 (1980)].

[16]L. P. Volkov, N. P. Voloshin, A. S. Vladimirov, V. N. Nogin, and V. A. Simonenko, Zh. Eksp. Teor. Fiz. Pis'ma Red. 31, 623 (1980) [Sov. Phys.—JETP Lett. 31, 588 (1980)].

[17]C. E. Ragan III, Phys. Rev. A 21, 458 (1980).

[18]C. E. Ragan III, in *High Pressure Science and Technology,* edited by B. Vodar and Ph. Marteau (Pergamon, New York, 1980), Vol. 2, pp. 993–999.

[19]C. E. Ragan III, Phys. Rev. A 25, 3360 (1982).

[20]C. E. Ragan, B. C. Diven, M. Rich, E. E. Robinson, and W. A. Teasdale, in Ref. 4, pp. 169–173.

[21]C. E. Ragan, in *High Pressure in Research and Industry,* edited by C.-M. Backman, T. Johannison, and L. Tegnér (Arkitektkopia ISBN, Uppsala, Sweden, 1982), Vol. 1, pp. 156–159.

[22]L. V. Al'tshuler, Usp. Fiz. Nauk 85, 197 (1965) [Sov. Phys.—Usp. 8, 52 (1965).

[23]C. E. Ragan III, M. G. Silbert, and B. C. Diven, J. Appl. Phys. 48, 2860 (1977).

[24]B. I. Bennett, J. D. Johnson, G. I. Kerley, and G. T. Rood, Los Alamos Scientific Laboratory report LA-7130 (unpublished); Los Alamos Scientific Laboratory brochure LASL-79-62 (unpublished); Equation-of-State and Opacity Group, Los Alamos National Laboratory brochure LALP-83-4 (unpublished).

[25]C. E. Ragan III, M. G. Silbert, A. N. Ellis, E. E. Robinson, and M. J. Daddario, Los Alamos Scientific Laboratory report LA-6946-MS (unpublished).

[26]Ya. B. Zel'dovich and Ya. P. Razier, *Physics of Shock Waves and High-Temperature Hydrodynamic Phenomena,* edited by W. D. Hayes and R. F. Probstein (Academic, New York, 1967), Vol. II, pp. 746–748.

[27]LASL Group X-6, Los Alamos National Laboratory report LA-7396-M, revised (unpublished).

[28]R. A. Graham, F. W. Neilson, and W. B. Benedick, J. Appl.

Phys. 36, 1775 (1965).
[29]G. I. Kerley, see Ref. 4, pp. 208—212.
[30]G. I. Kerley, in *Proceedings of Eighth Symposium on Thermophysical Properties, Vol. II: Thermophysical Properties of Solids and Selected Fluids for Energy Technology,* edited by Jan V. Sengers (American Society of Mechanical Engineers, New York, 1981), pp. 159—164.
[31]K. S. Trainor, in H-Division Quarterly Report, April through June 1982, Lawrence Livermore National Laboratory report UCID-18574-82-2 (unpublished).
[32]G. I. Kerley (private communication).
[33]G. I. Kerley, Los Alamos report LA-8833-M (unpublished).
[34]G. I. Kerley, in *Molecular Based Study of Fluids,* edited by J. M. Haile and G. A. Mansoori (American Chemical Society, Washington, D.C., 1983), pp. 107—138.
[35]A. K. McMahan, in *High Pressure in Research and Industry,* edited by C.-M. Backman, T. Johannisson, and L. Tegnér (Arkitektkopia ISBN, Uppsala, Sweden, 1982), Vol. 2, pp. 453—459, and references therein.